Multiparametric Magnetic Resonance Imaging Study of Huntington's Disease

Ricardo Nuno Vieira Leitão

Instituto Superior Técnico, University of Lisbon, Lisbon, Portugal
e-mail: ricardo.v.leitao@tecnico.ulisboa.pt

ABSTRACT

Huntington's Disease (HD) is an autosomal-dominant and fatal neurodegenerative disorder, caused by an expanded trinucleotide repeat in the huntingtin gene. HD displays as a triad of worsening motor, cognitive and psychiatric symptoms, resulting from widespread neuronal dysfunction and cell death. Although genetic testing allows for identification of affected individuals before symptomatic onset, no current therapies can delay HD progression. This cross-sectional study was aimed at comparing multiple structural magnetic resonance imaging parameters in 8 HD patients and 12 healthy controls, in the pursuit of objective and quantitative biomarkers to track disease progression. Firstly, the volumes of several subcortical structures were quantified in T1-weighted images using an automated segmentation approach. Neuromelanin (NM) content in the substantia nigra pars compacta (SNc) was estimated using a semi-automatic segmentation method in NM-sensitive images. The iron content of the basal ganglia was also quantified using R2* relaxometry. Comparing to controls, HD patients showed significant volume reduction in the caudate nucleus, putamen, globus pallidus, brainstem and midbrain, and an enlargement of the lateral ventricles. Caudate and putamen volumes of HD patients correlated significantly with their total motor and total functional capacity (TFC) scores. R2* values in the basal ganglia of HD patients were not significantly different from those of controls and did not correlate with volumes of these structures. SNc areas of HD patients were significantly reduced and correlated with their TFC. The SNc areas correlated significantly with all basal ganglia volumes, suggesting that SNc degeneration and basal ganglia atrophy may not be independent processes.

Keywords: Huntington's disease; structural magnetic resonance imaging; neuromelanin; neurodegeneration; relaxometry; volumetry.

1. Introduction

Huntington's Disease (HD) is a progressive, autosomal dominantly inherited and fatal neurodegenerative disorder, manifested as a triad of gradually worsening motor, cognitive and psychiatric symptoms. The most prominent manifestation of this disease is chorea, which consists of rapid dance-like involuntary movements [1]. Despite being considered a rare disease, HD is the most common monogenic neurological disorder in the world [1], with a global prevalence of 5.5 cases per 100,000 population [2].

HD is caused by a mutation of Cytosine-Adenine-Guanine (CAG) expansion in the HTT (huntingtin) gene that codes for the huntingtin protein, located in chromosome 4, such that the number of CAG repeats in this gene exceeds 35 [3]. Since the CAG trinucleotide codes for the glutamine amino acid, a translation of polyglutamine tracts into the protein takes place, resulting in a mutated form of huntingtin, which misfolds and aggregates into inclusion fibrillar bodies by unknown mechanisms [4]. These aggregates are believed to be the initiators of the complex pathological cascade of HD, as they prompt transcription dysregulation of several genes, synaptic dysfunction and increased oxidative stress, among several other pathological processes [5]. Such pathogenesis mechanism constitutes a hallmark of the disease that places HD alongside other neurodegenerative disorders similarly characterized by protein aggregates, such as Parkinson's Disease (PD) and Alzheimer's Disease (AD) [4]. However, HD is unique in the sense that it is caused by a single mutation for which genetic testing is available [6], allowing the preclinical diagnosis to be performed prior to the onset of clinical manifestations. The onset of HD is the point in time when an individual who carries a known CAG-expanded huntingtin allele (or has a family history of HD) develops motor symptoms that are unequivocal signs of HD [7].

In HD, although mutant huntingtin is ubiquitously expressed in the human brain, primary neurodegeneration occurs in the caudate-putamen (striatum) and in the cerebral cortex. The neuropathological hallmark of HD is a progressive bilateral degeneration of the striatum due to the demise of Medium Spiny Neurons (MSNs), which starts up to 15 years prior to onset of motor symptoms, and steadily progresses thereafter [8]. MSN loss is accompanied by the death of Cortical Pyramidal Neurons (CPNs), primarily in motor and premotor areas, albeit to a lesser extent. A dysfunction in the patterns of communication between these two types of neurons, which are major players in the corticostriatal pathway, is thought to occur even before neuronal death. The corticostriatal pathway encompasses the striatum and the Globus Pallidus (GP) (which together comprise the basal ganglia), the cerebral cortex, the

subthalamic nucleus, the thalamus and the Substantia Nigra (SN). According to the corticostriatal pathway model, the striatal MSNs integrate glutamatergic (excitatory) cortical inputs and relay that information to downstream nuclei through the direct and indirect corticostriatal pathways, which act in opposite ways to control movement. Voluntary movement is initiated by the direct pathway and inhibited by the indirect pathway. Excitatory projections from the cortex are not the only influence on basal ganglia circuitry. Dopaminergic projections from the substantia nigra *pars compacta* (SNc) to the striatum play a modulatory role in the corticostriatal pathway, by exciting the direct pathway and inhibiting the indirect pathway, ultimately resulting in facilitation of movement. Therefore, a dysregulation of dopamine would result in uncontrollable involuntary movements [9]. In adult-onset HD (mean age at HD onset of 40 years), MSNs in the indirect pathway are preferentially lost prior to MSNs of the direct pathway, creating an imbalance between both circuits. The consequence is the inability to control voluntary movement, resulting in hyperkinetic choreatic movements. Direct MSNs are generally affected in the later stages of the disease, leading to movement impairment such as rigidity, incoordination or bradykinesia (slowness of movement), usually when choreatic movements reach a plateau or start to fade. In contrast to adult-onset HD, chorea is not a major manifestation of juvenile-onset HD, and motor impairment along with seizures seem to be the predominant features of this variant of HD (Westphal HD). Juvenile HD is defined by the onset of symptoms before the age of 20, by a more severe and rapid neuropathological involvement than adult-onset HD, and accounts for 5 to 10% of HD cases [10].

Impaired corticostriatal connectivity and neuronal cell death of MSNs and CPNs, beginning before HD onset, thus set the stage for the emergence of HD symptoms [11]. Subsequent to striatal atrophy and in a lesser magnitude, volume loss also occurs in other subcortical structures and propagates to cortical gray matter (GM) and to white matter (WM), culminating in a widespread neurodegeneration in the later stages of HD. Nonetheless, no current therapies can forestall symptomatic onset nor slow disease progression, which leads to death up to 20 years after onset [1].

The Unified Huntington's Disease Rating Scale (UHDRS) [12] is currently the most widely used tool in clinical practice for the assessment of HD progression. It consists of four components evaluating motor function, cognition, behavior and functional capacities. The UHDRS-Total Motor Score (TMS) is a clinical rating subscale assessing multiple domains of motor disability in HD. More specifically, 31 motor signs of the disease are evaluated in this scale, including eye movement, oropharyngeal dysfunction, hand coordination, rigidity, bradykinesia, chorea and balance. Each of these items is rated from grade 0 (not affected) to grade 4 (most severely affected), adding to a maximum of 124 points in the TMS scale [13]. One of the most frequent measures of function in HD patients is the UHDRS-Total Functional Capacity (TFC) scale, which assesses occupation, ability to perform domestic chores, daily activities and level of care of HD patients. Scores on these five items, attributed by the clinician, are summed to yield a TFC ranging from 0 to 13, with 0 corresponding to severe functional capacity deterioration while greater scores indicate higher functional capacity [14].

However, as in any clinical scale, UHDRS is subject to inter-rater variability. Additionally, it requires extensive training to achieve reliability among raters. There is, therefore, a pressing need for a panel of robust and objective biomarkers capable of monitoring disease progression and determining drug efficacy in clinical trials, in the search of disease-modifying therapies. Nevertheless, there is yet no validated imaging biomarker for the study of HD progression [15]. Neuroimaging methods have offered, so far, the most robust biomarkers for this disease [16].

Volumetry analyses using structural magnetic resonance imaging (MRI) techniques have been extensively used to confirm the volume reductions of several brain structures in HD patients, namely of the caudate, putamen and GP nuclei of the basal ganglia [17],[18]. Furthermore, correlations between striatal volumes and disease duration [18], TFC and other clinical scores have been reported [15], implicating striatal degeneration in symptom manifestation in HD. Extra-striatal atrophy was also reported in the nucleus accumbens [19], hippocampus [19], amygdala [20], brainstem [19], thalamus [20], cerebral WM [19] and in the GM [20] of HD patients. Moreover, an increase of over 100% in the volume of the lateral ventricles of HD patients was found in [19].

R_2* relaxometry and magnetic susceptibility-related measures such as quantitative susceptibility mapping (QSM) have been used in several MRI neuroimaging studies of HD. A potential pathological feature of HD is a disruption of brain iron homeostasis caused by the agglomerates of mutant huntingtin, leading to iron accumulation in the basal ganglia. Iron overload generates oxidative stress which results in neuronal damage, ultimately prompting the death of affected neurons. Both the R_2* and the magnetic susceptibility values strongly correlate with iron content [21],[22]. Previous studies have collectively reported higher iron accumulation in the caudate, putamen and GP in HD patients, but their results were not always consistent. Using R_2* relaxometry, [23] reported increased iron in the GP of HD patients, while in [24] increased iron was detected in both the GP and the putamen. On the other hand, a QSM study [25] revealed increased iron content in the caudate and putamen of HD patients, while another reported increased iron in all basal ganglia structures [26] using the same technique. Therefore, the pattern of iron accumulation in the basal ganglia of HD patients is not yet understood. Some groups have found significant correlations between iron and volume of the basal

ganglia of HD patients [24],[25], but it is still not known whether iron deposition precedes or depends on basal ganglia atrophy.

The dopaminergic neurons of the SNc, which provide modulatory input to the basal ganglia through the striatum in the corticostriatal pathway, contain neuromelanin (NM), a highly paramagnetic dark pigment with a major role in maintaining iron homeostasis [27]. Considering said features of this midbrain structure, the loss of striatal volume, the possible disruption of iron homeostasis in HD and the debilitation of the motor function in the disease, it would not be surprising if degeneration of the SNc and the consequent NM depletion are somehow involved in the pathological cascade of HD. Indeed, an *in vitro* study [28] revealed a decreased cross-sectional area of the SN, a reduction in the number of neurons in the SNc and a depletion in the amount of intraneuronal melanin in the SNc of HD patients. Furthermore, SN volume reduction in HD patients was reported in one MRI study [20], but the *pars compacta* and the *pars reticulata* of the SN were not analyzed separately. To date, as far as we know, no study has quantitatively assessed the NM in the SNc of HD patients with MRI.

The SNc can be visualized *in vivo* using neuromelanin-sensitive magnetic resonance imaging (NM-MRI) techniques. NM-MR images obtained with Fast Spin Echo (FSE) sequences similar to that of [29] rely on the magnetization transfer (MT) contrast to display the bilateral SNc as two band-like high signal areas in cerebral peduncle at the level of the midbrain, as exemplified in Figure 1.

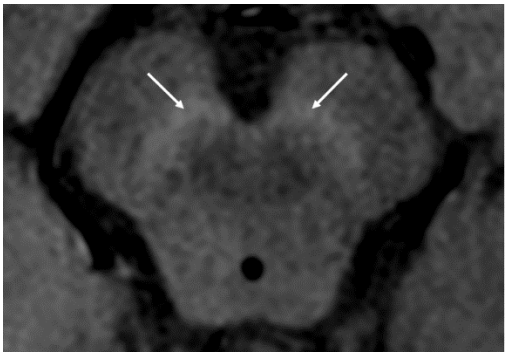

Figure 1: Section of an axial slice of a NM-MR image at the level of the centre midbrain displaying the bilateral SNc as an hyperintense band-like area (pointed by the white arrows).

The MT effect consists in the shifting of energy between the protons contained in macromolecules and membranes of tissues (bound protons) and the mobile water protons (free protons). In multi-slice FSE sequences, the off-resonance radiofrequency (RF) radiation from several 180º refocusing pulses selectively saturates bound protons. Bound protons transfer their magnetization to the free protons, accelerating spin dephasing and thus leading to a reduction of the signal intensities produced by the latter. NM-containing SNc, due to its highly paramagnetic properties, will not be significantly affected by MT effects, thus this structure will be hyperintense in NM-MRI images comparing to the suppressed background tissues.

The aims of this cross-sectional, multiparametric structural MRI study of HD were (1) to investigate the volume changes in several subcortical structures of HD patients comparing to healthy controls (HCs); (2) to quantify single-slice SNc areas and contrast ratios in NM-MR images of HD patients, as indirect measures of the NM content in their SNc; and (3) to evaluate iron content in the basal ganglia of HD patients using quantitative R2* relaxometry. This work also aimed at investigating the relations of all the parameters with the clinical parameters of HD patients: disease duration, TMS and TFC. Finally, the relations between the volumes of the basal ganglia and SNc areas were assessed, as well as the relationship between basal ganglia volume and iron.

2. Methods

2.1 *Sample Description*

This study consisted of a cross-sectional case-control analysis including 20 subjects: 8 HD patients with abnormal CAG repeats (≥36) and 12 healthy individuals. HD patients were recruited from the Movement Disorders Unit of the University Hospital of Santa Maria-Lisbon. All patients were diagnosed by a movement disorders specialist (Dr. Leonor Correia-Guedes) and were scored for motor (TMS) and functional capacity (TFC) according to the UHDRS. The clinical characteristics of all subjects are displayed in Table 1. One patient with 27 years of age had Westphal HD.

Table 1: Demographic and clinical characteristics of the sample. For numerical characteristics the median (range) values are shown.

	HD (n=8)	**HC (n=12)**	**P-value†**
Gender (M:F)	3:5	7:5	0.40
Age (y)	46 (27 – 81)	62 (49 – 83)	0.02
Dis. Duration (y)	7.5 (1 – 16)	-	-
TMS	20 (4 – 71)	-	-
TFC	12 (1 – 13)	-	-

† P-values obtained with the Mann Whitney U test. Dis.:Disease.

2.2 *Imaging Protocol*

An MRI protocol including a T_1-weighted 3D Turbo Field Echo (TFE) sequence with an inversion recovery pulse, a NM-MRI 2D multi-slice FSE sequence and a T_2*-weighted multi-echo Fast Field Echo (mFFE) sequence was performed using a 3 T Philips scanner (Philips Achieva; Philips Medical Systems, Best, Netherlands) with an 8-channel head coil. The sequence parameters are displayed in Table 2. In the mFFE sequence, seven T_2*- weighted image volumes with a partial Fourier of 80% were acquired with equally spaced TEs, with a spacing of 4.7 ms, starting from 13.8 ms.

*Table 2: Sequence parameters for the imaging protocol used in this study. FOV: Field of View, TE: Time of Echo, TR: Time of Repetition. *The T_2*-mFFE sequence included seven equally spaced echoes with a spacing of 4.7 ms, starting from 13.8 ms.*

Sequence	TR (ms)	TE (ms)	Pixel Size (mm^2)	Sl. Thickness (mm)	FOV (mm^2)	No. Slices	Acq. Time (m:s)
T_1-TFE	9.6	4.6	0.49x0.49	1.0	250x250	151	05:25
T_1-FSE	607	10	0.40x0.40	2.5	220x190	20	08:20
T_2*- mFFE	1405	13.8;18.5;…*	0.90x1.12	4.0	240x180	28	03:48

2.3 *Volumetry Analysis*

The volumetry analysis was carried out with the FreeSurfer software (v.6.0; The General Hospital Corporation, Boston, MA, USA). All T_1-weighted anatomical images were preprocessed using the *recon-all* command. These images underwent intensity normalization to correct for image intensity variations (or bias fields) due to magnetic susceptibility artifacts and RF-field inhomogeneities. The neck and skull were stripped, and the brain was registered with the Montreal Neurological Institute (MNI) space. Segmentation of several brain structures of the subjects was then automatically performed based on a probabilistic atlas from a manually labeled data set incorporated in FreeSurfer [30]. This segmentation procedure yielded the volumes of the segmented structures of interest for each subject: caudate, putamen, GP, lateral ventricles and intracranial volume (ICV, comprising the GM, WM and cerebrospinal fluid - CSF). Examples of the subcortical segmentation masks of the basal ganglia and of the ventricles are displayed in Figure 2. To segment and quantify the volumes of the midbrain and the brainstem, the *BrainstemSubstructures* tool [31] was used in FreeSurfer.

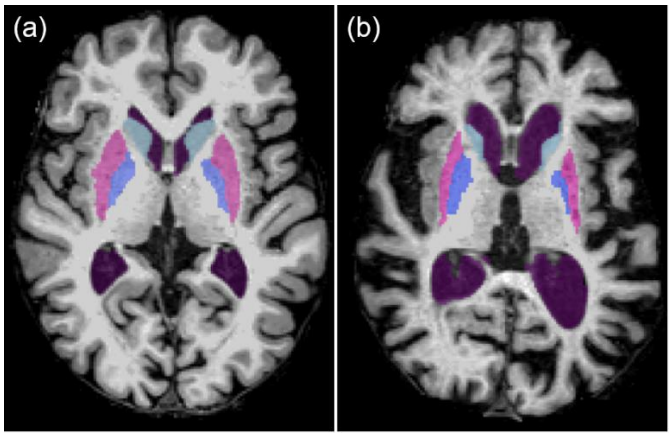

Figure 2: Axial slices of T_1-weighted images of a HC (a) and of a HD patient (b), with subcortical segmentation masks: the caudate nucleus (in light blue), the putamen (in pink), the GP (in dark blue) and the lateral ventricles (in deep purple). Note the clear reduction of the basal ganglia mask size and the ventricle enlargement in (b) comparing to (a).

Each resulting volume was divided by the ICV of each subject, yielding the relative volume of the structure. This was done to allow for the comparison of volumes between subjects while accounting for overall differences in brain volumes. To evaluate the relative changes in the brain volumes of HD patients when comparing to HCs, the mean relative volume of each structure of HD patients was divided by that of HCs.

2.4 *NM-MRI Analysis*

Analysis of neuromelanin-sensitive images was conducted with the OsiriX software (v. Lite 9.5; Pixmeo, Geneva, Switzerland). For each subject, from the 20 axial slices obtained with the imaging protocol, only three exhibited the NM hyperintense signal corresponding to the SNc. The middle slice, containing the largest area of high-signal SN, was selected for analysis. A *Gaussian Blur* convolution filter with a 5x5 kernel dimension and a full width at half maximum (FWHM) of 2 pixels was applied to the image to compensate for its low signal-to-noise (SNR) ratio. The *Confidence* algorithm was then used to perform SNc segmentation. This region-growing algorithm starts from the selection of a seed point and it progressively appends neighboring pixels to the current region if their intensities $I(X)$ are included in a confidence interval iteratively updated by the statistics of the current region:

$$I(X) \in [m - f\sigma, m + f\sigma] \quad (1)$$

where m and σ are, respectively, the mean and standard deviation of the intensities for all pixels in the current region, and f is a multiplicator factor defined by the user. The iteration stops when the algorithm visits all pixels neighboring the current region. Then, m and σ of the new ROI are calculated, and another iteration begins. Besides seed point placement, the algorithm required three input parameters: the multiplier factor (set to 2), the number of iterations (set to 2) and the so-called initial radius (set to 1 pixel). The choices of these parameters, of the *Confidence* algorithm for SNc segmentation, and of the *Gaussian Blur* filter were all based on a previous work [32], which focused on optimizing the method for segmentation of the SNc in NM-MR images obtained with the same sequence used in this study.

The method for seed point placement consisted of drawing a line crossing the interpeduncular fossa and selecting a hyperintense SNc pixel along such line, as exemplified in Figure 3 (a). After application of the Confidence algorithm on the selected seed point, SNc segmented regions usually presented small gaps of pixels within the region of interest (ROI), as shown in Figure 3 (b). To avoid anatomically implausible discontinuities in the SNc, a *Brush Closing* filter

was applied whenever required, resulting in continuous ROIs, as displayed in Figure 3 (c). For each subject's single-slice filtered image, the semi-automatic segmentation procedure was executed once for each side of the brain, adding to a total of 40 SNc areas.

Although this semi-automatic segmentation method was proven to be accurate for PD patients in [32] and in [33] comparing to manual segmentations, its accuracy was never tested in HD patients. Furthermore, by reproducing the procedure a few times in this work, variability of the segmented area values associated with seed point selection was still observed, despite image filtering. Therefore, manual segmentation of the SNc was also performed to confirm the accuracy of the semi-automatic segmentation method when applied to this patient group.

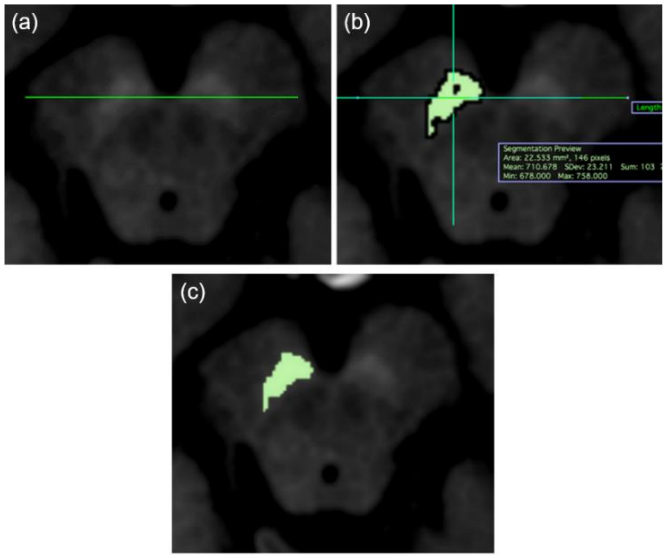

Figure 3: Semi-automatic SNc segmentation method using the Confidence algorithm after application of a Gaussian Blur filter. A line is drawn crossing the interpeduncular fossa (a). A hyperintense pixel along the line is chosen and the algorithm generates the ROI (b). Then, the Brush Closing filter is applied to ensure that the selected SNc area is completely filled (c). Adapted from [33].

Manual segmentation was done once for each SNc in a different day from the corresponding semi-automatic segmentation to prevent biasing. The manual SNc ROIs was confirmed by a certified neuroradiologist (Dr. Sofia Reimão). The evaluation of the accuracy of semi-automatic image segmentation was then carried out using the Dice Similarity Coefficient (DSC), which quantitatively measures the spatial overlap between the two segmentations:

$$DSC = 2\frac{|SN_{sa} \cap SN_m|}{|SN_{sa}| + |SN_m|} \quad (2)$$

where SN_{sa} represents the SNc area obtained using the semi-automatic segmentation and SN_m is the SNc area manually delineated.

The midbrain was manually segmented so as to obtain the global midbrain area. The ratio of SNc to midbrain area was calculated for each side of the brain as SN_{area}/M_{area}, where SN_{area} is the SNc area and M_{area} is the midbrain area. This parameter, hereafter termed SNc ratio, allowed for a comparison of SNc areas while taking into account inter-subject anatomical variability.

The contrast ratio (CR) between the hyperintense SNc area and a background reference ROI was determined to assess the distribution of NM in the SNc. Circular ROIs of 8 mm^2 were placed bilaterally in the *crus cerebri* as references, as shown in Figure 4. The right and left CRs of each subject, CR_r and CR_l respectively, were calculated as:

$$CR_r = \frac{I_{SN_r}}{I_{CC_r}} \quad (3)$$

$$CR_l = \frac{I_{SN_l}}{I_{CC_l}} \quad (4)$$

where I_{SN_r} and I_{SN_l} are, respectively, the mean intensities of all the pixels contained in the right and left SNc areas, and I_{CC_r} and I_{CC_l} are the mean intensities of pixels included the left and right reference ROIs. The CR analysis was performed with no filter applied to the image.

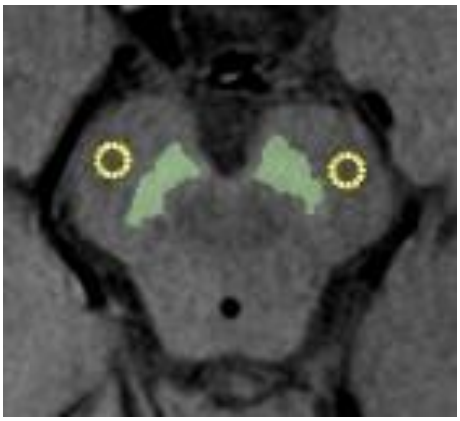

Figure 4: Method used to calculate the CRs of SNc areas in non-filtered NM-MR images. For each side of the midbrain, an 8 mm^2 circular ROI (in yellow) was placed in the central region of the crus cerebri .The CR was determined by dividing the mean intensity of the pixels contained in each SNc area (in green) by the mean intensity of the pixels included in the corresponding reference ROI.

2.5 *R_2*-Relaxometry Analysis*

T_2*-weighted image processing was performed with FSL (FMRIB Software Library v6.0; Analysis Group, Oxford, UK). For each subject, FSL's brain extraction tool (BET) was used to strip the skull and neck of the first echo (TE=13.8 ms), which had the highest contrast-to-noise ratio of the T_2*-weighted volume series. A resulting binarized brain mask was then applied to the volumes of the six remaining echoes. FMRIB's Automated Segmentation Tool (FAST) was then applied to each skull-stripped volume to correct for bias field. Afterwards, the resulting volumes were merged into 4D image files, which contained the seven volumes of the pre-processed echoes. For each subject, this 4D image was used to perform a voxel-wise nonlinear least squares fitting to the data acquired at the seven TEs with Matlab (v.9.1 R2016b; The Mathworks, Natick, MA,

USA), as exemplified in Figure 5, considering a monoexponential signal decay curve model according to the T2* relaxation:

$$S(TE) = S_0 e^{-\frac{TE}{T_2^*}} \quad (5)$$

where S is the measured signal intensity for each echo, S_0 reflects the proton density and the scanner receiver gain, TE is the echo time and T_2* is the apparent relaxation time. Ultimately, an image containing a T_2* value for each voxel, or a T_2* map, was obtained for each subject. R_2* maps (R_2*=1/T_2*) were computed for each subject from the T_2* maps.

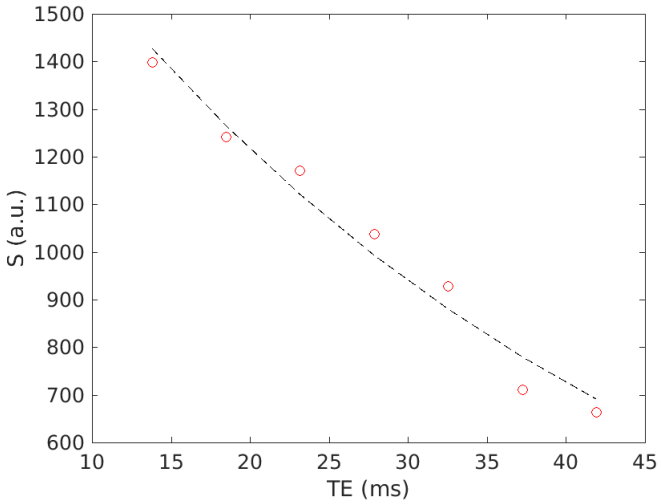

Figure 5: Example of a monoexponential signal decay curve fitted to the data corresponding to one voxel. The red circles correspond to the measured signal values in arbitrary units for each of the seven TEs. The dashed line represents the exponential decay as a function of TE, obtained after nonlinear fitting of the measured data in this voxel (T_2= 39 ms, R_2*=26 s^{-1}).*

In parallel, using the boundary-based registration of the *epi_reg* function in FSL, the pre-processed first echo was registered to the high-resolution skull-stripped T_1-weighted volume previously generated by FreeSurfer, so as to obtain the registration matrix for the T_2*-to-T_1 transformation. Subsequently, the segmentation masks of the basal ganglia formerly obtained with FreeSurfer were transformed to the space of the T_2*-weighted volume series using FMRIB's Linear Image Registration Tool (FLIRT) with the inverse of the T_2*-to-T_1 transformation matrix, calculated in the previous step.

Afterwards, the basal ganglia masks in the T_2*-space were binarized and multiplied with the total R_2* maps, yielding regional R_2* maps of the caudate, putamen and GP of each subject. Since the caudate is adjacent to the CSF in the lateral ventricles, some voxels included in the caudate mask could have overlapped with the CSF, which has much lower R_2* values. Therefore, voxels belonging to this tissue were excluded from the caudate masks in order to avoid underestimation of R_2* values in this structure. Examples of a total R_2* map and of regional basal ganglia R_2* maps are shown in Figure 6.

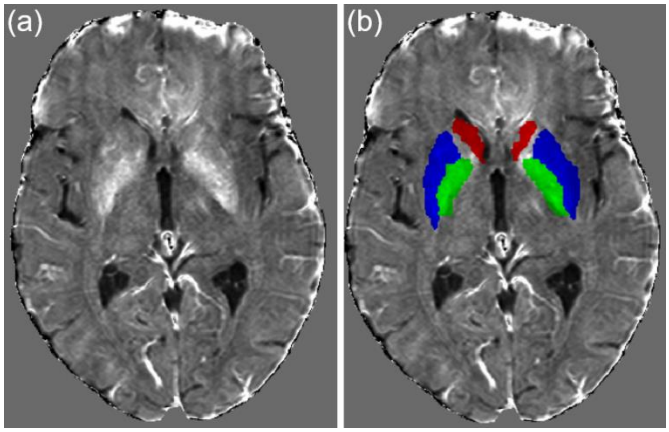

Figure 6: R_2 map of an axial slice of a HC (a), overlapped with the R_2* regional maps of the basal ganglia in (b): the head of the caudate (in red), the putamen (in blue), and the GP (in green). These masks were generated by FreeSurfer and registered to the space of the first echo of the T_2*-weighted images using FSL's FLIRT.*

2.6 Statistical Analysis

All statistical analyses were performed with non-parametric tests in R (v.3.5.1; R Foundation for Statistical Computing, Vienna, Austria). A p-value lower than 0.05 was considered significant. The Wilcoxon signed rank test for paired samples was used to assess side-wise differences in parameters measured in each brain hemisphere, in each cohort of subjects. This statistical test was also used to investigate differences between the values of manual SNc areas and semi-automatic SNc areas. Regarding left and right-sided parameters, whenever no significant difference was found between both values, the average value was henceforth used.

Differences in the parameters between HD patients and HCs were evaluated with the Mann-Whitney U test. The Spearman rank-order correlation test was used to investigate correlations between the parameters of HD patients and three available clinical variables: disease duration, TMS and TFC. Correlations of basal ganglia volume with SNc ratios and with R_2* values were also assessed with this test.

3. Results

3.1 *Volumetry Analysis*

No statistically significant differences were found among the volumes of the left and right caudate, putamen, GP and lateral ventricles in each cohort (p-values>0.05), except in the caudate nucleus of HCs. The volumes of the right-sided caudate were significantly larger (p<0.005) than those of the left-sided structure in this cohort.

The relative volumes of the basal ganglia of HCs and HD patients are shown in Figure 7. The relative volumes of the brainstem, midbrain and lateral ventricles are displayed in Figure 8. Significant reductions in the left, right and averaged caudate (mean percent change of -35%; p<0.001), putamen (-36%; p<0.05), GP (-28%; p<0.01), brainstem (-18%; p<0.05) and midbrain (-19%; p<0.05) volumes were detected in the HD

cohort. A significant increase in the volumes of the ventricles (+96%; p<0.05) of HD patients was also detected.

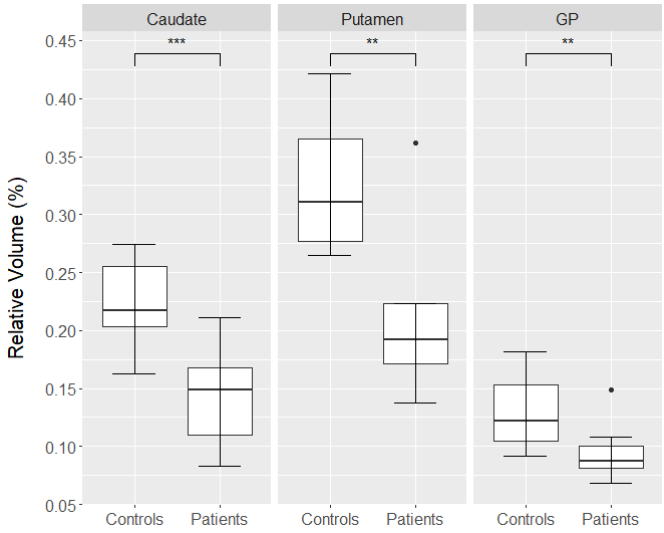

*Figure 7: Volumes of the basal ganglia relative to the ICV of HCs and subjects with HD. Significant reductions were found in the relative volumes of the caudate (*** p<0.001), the putamen and of the GP (** p<0.01) in HD patients with the Mann Whitney U test.*

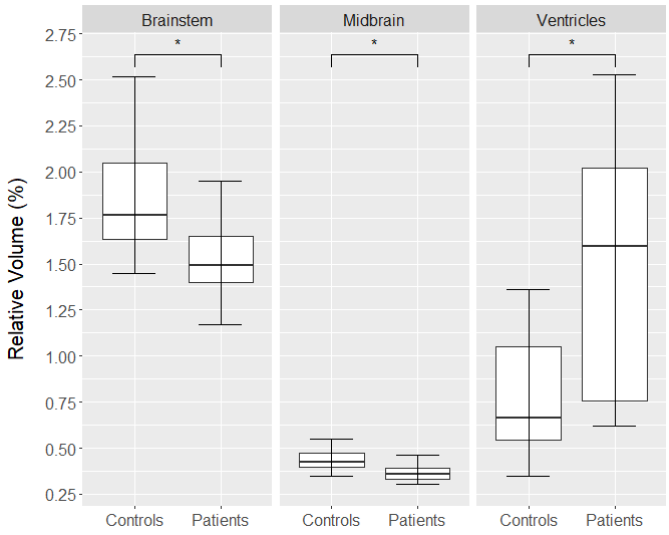

Figure 8: Volumes of the brainstem, midbrain and lateral ventricles relative to the ICV of HCs and subjects with HD. Significant reductions in the relative volumes of the brainstem and of the midbrain, and a significant increase in the volume of the lateral ventricles (p<0.05) of HD patients were found with the Mann Whitney U test.*

Caudate volumes correlated significantly with both the TMS ($r_S = -0.71$ with p<0.05) and the TFC ($r_S = 0.82$ and p=0.01). Putamen volumes also correlated significantly with the TMS ($r_S = -0.76$ with p=0.03) and the TFC ($r_S = 0.81$ and p=0.02), while the correlations of the caudate and putamen volumes with disease duration did not reach statistical significance ($r_S = -0.64$ and p=0.09 for both structures). No significant correlations were found between the remaining volumes and the clinical scores (p-values > 0.05).

3.2 *NM-MRI Analysis*

For all subjects, the DSC obtained between the semi-automatic and manual SNc segmentations was 0.78 [0.59 – 0.88] (median; range), which reveals a very good spatial overlap between the areas. Furthermore, no statistically significant difference was found when comparing the semi-automatically and manually segmented SNc area values (p = 0.83). Considering the healthy subjects, no significant differences were revealed between their left and right-sided SNc areas, obtained with either the semi-automatic (p=0.08) or the manual (p=0.97) segmentation methods. Regarding HD patients, no significant side-wise differences were found in their SNc area values either, delineated using the semi-automatic (p=0.20) or manual (p=1.0) segmentations. Given the excellent agreement between semi-automatic and manual SNc areas revealed by the similarity analysis and by the comparison of area values, only the SNc areas obtained with the semi-automated segmentation method were henceforth considered.

The SNc and midbrain areas are represented in Table 3, along with the SNc ratio, for each cohort of subjects. Significant reductions were detected in the SNc areas (p<0.005), in the midbrain areas (p<0.01) and in the SNc ratios (p<0.01) of subjects with HD comparing to HCs.

Table 2: Median (range) values of the SNc areas, midbrain areas and SNc ratios of HCs and of subjects with HD. P-values were obtained with the Mann-Whitney U-test, which show statistically significant differences for p<0.05. MB: Midbrain

Parameter	HCs	HD Subjects	P-Value
SNc Area (mm^2)	35 (22-50)	25 (17-36)	<0.005
MB Area (cm^2)	6.6 (5.6-7.6)	5.7 (5.0-7.5)	<0.01
SNc Ratio (%)	5.2 (3.5-7.4)	4.4 (3.1-5.1)	<0.01

No significant asymmetry in the CR values was found either in HCs ($p = 0.20$) or in subjects with HD ($p = 0.74$). Regarding HCs, a CR value of 14% (11%-17%) [median; range] was obtained, while for the HD cohort, a CR value of 13% (8%-16%) was found. Although CR values of HD patients tended to be smaller, this parameter did not allow to significantly distinguish controls from patients ($p = 0.57$).

The correlations of SNc ratios to disease duration ($r_S = -0.25$; $p = 0.56$), TMS ($r_S = -0.43$; $p = 0.29$) and TFC ($r_S = 0.60$; $p = 0.12$) were not statistically significant. There were considerable correlations of the values of SNc areas with disease duration ($r_S = -0.60$) and TMS ($r_S = -0.67$), but they did not reach statistical significance ($p = 0.12$ and $p = 0.07$, respectively). On the other hand, a statistically significant, strong positive correlation between SNc areas and the TFC score of subjects with HD was found ($r_S = 0.79$, $p = 0.02$).

The SNc ratio correlated significantly with the relative volume of the caudate ($r_S = 0.58$, $p = 0.009$), of the putamen

($r_S = 0.66$, $p = 0.002$ as shown in Figure 9) and of the GP ($r_S = 0.67$, $p = 0.002$).

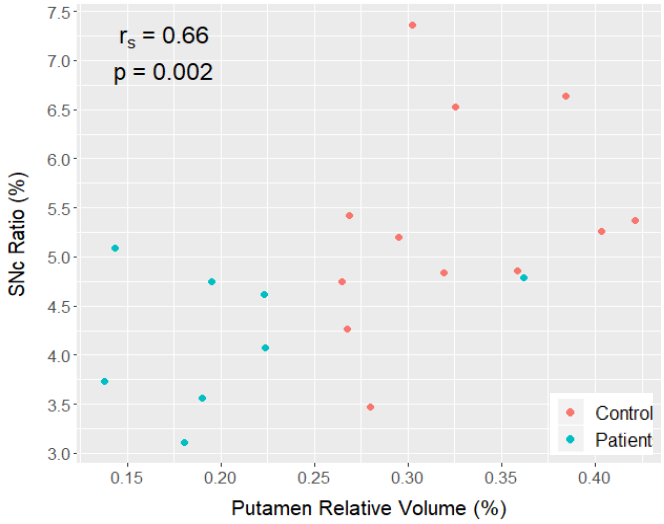

Figure 9: SNc ratios of all subjects plotted against their relative putamen volume. A statistically significant positive correlation between both variables was found with the Spearman's correlation test ($r_S = 0.66$, $p = 0.002$).

3.3 *R_2*-Relaxometry Analysis*

The R_2* relaxometry analysis was performed on the T_2* data of a sample of 11 HCs and 5 HD patients. The reasons for having smaller group sizes are that T_2* mFFE data were not acquired for two HD patients, and the poor quality of the T_2*-weighted images of a third patient and of a HC made their analyses unfeasible due to motion artifacts.

No significant differences were found between the R_2* values of the left and right structures in each cohort (p-values>0.05), except in the case of the caudate of HCs. The R_2* values of the left-sided caudate were significantly larger ($p < 0.01$) than those of the right caudate in this cohort.

No significant differences were found in the R_2* values between the left caudate structures ($p = 0.66$) and between right caudate structures ($p = 0.38$) when comparing HD patients to HCs. R_2* values of each structure for each cohort are displayed in Table 4. No significant differences were found in the R_2* values of the caudate ($p = 0.44$), putamen ($p = 0.58$) and pallidum ($p = 0.32$) between HCs and subjects with HD.

In order to assess the relation of age with iron content in basal ganglia structures, the Spearman's correlation test was applied between the R_2* values in the caudate, putamen and GP, and the age of healthy subjects included in this analysis. Only the R_2* values in the caudate significantly correlated with age ($r_S = 0.65$; $p = 0.03$).

Regarding the relation of iron content in the basal ganglia of HD patients with the clinical characteristics, the only statistically significant correlation detected was between iron content in the GP with the TFC score ($r_S = 0.95$, $p = 0.01$). A trend towards significance was, however, revealed between the R_2* values in the GP and disease duration ($r_S = 0.87$, $p = 0.05$).

No significant correlations were found between R_2* values and relative volumes of the basal ganglia, although a trend towards statistical significance was detected in the correlation between the iron content and relative volume of the caudate in this cohort ($r_S = -0.49$; $p = 0.06$).

Table 3: R_2 (range) values of the basal ganglia structures of HCs and subjects with HD. P-values were obtained with the Mann-Whitney U-test, which show statistically significant differences for p<0.05.*

Structure	HCs - R_2* (s^{-1})	HD - R_2* (s^{-1})	P-Value
Caudate	25 (22-27)	25 (24-29)	0.44
Putamen	31 (28-34)	31 (29-32)	0.58
GP	41 (34-53)	42 (41-52)	0.32

4. Discussion

4.1 *Volumetry Analysis*

The neuropathological hallmark of HD is striatal atrophy, which arises several years before symptomatic onset and progresses steadily over the course of the disease. In line with this and with the volumetric results from several MRI studies in HD [20],[23],[24], significant volume reductions in the caudate (-35%) and putamen (-36%) were detected in HD patients in this work. GP atrophy in these subjects was also significant, but less prominent (-28%) when comparing to atrophy in the caudate and putamen, in agreement with a previous study [19]. The caudate, putamen and GP are connected as part of the corticostriatal pathway and these structures are cardinal in the regulation of voluntary and involuntary movement. The degeneration of MSNs directly affects the basal ganglia, resulting in an imbalance of the corticostriatal pathway. Since the caudate, putamen and the GP are part of both the direct and the indirect circuits, degeneration of these structures is suggested to play a role in the movement abnormalities seen in HD [9]. Indeed, even with the small sample size of HD patients (n=8), significant strong correlations were found between the TMS and the volumes of the caudate (-0.71) and of the putamen (-0.76). Additionally, a correlation of the volumes of these structures with the TFC (-0.81 and -0.82 for the caudate and putamen, respectively) also implicates the atrophy of the striatum in the loss of functional capacity of HD patients. These results support the centrality of striatal atrophy in the pathology of HD.

Significant brainstem and midbrain volume reductions in HD patients were also detected in this study, in accordance with the results from previous works [19],[34]. The involvement of brainstem degeneration in HD is not among the established features of this disease, unlike basal ganglia atrophy. Indeed, Rüb et al. [34] have found evidence that brainstem atrophy develops independently from the well-documented striatal degeneration, suggesting that HD is not restricted to neurodegeneration in the striatum, cortex and corticostriatal

pathway, but is rather a multisystem neurodegenerative disorder. Brainstem degeneration in HD is thought to play a role in the manifestation of abnormal extraocular eye movements and sleep disturbances in these patients [19]. The volume of the lateral ventricles was significantly increased in HD patients, as a result of the loss of brain mass (hydrocephalus *ex vacuo*), which is consistent with the findings in [19].

The automatic subcortical segmentation technique used in this work employed a registration procedure robust to anatomical variability with enough sensitivity to detect alterations in volumes related to neurodegenerative diseases, and it was shown to yield results comparable in accuracy to manual labelling [30]. Moreover, only a single command was required for the preprocessing and brain segmentation of T_1-weighted images, meaning that virtually no *a priori* knowledge of brain anatomy is required for the labelling of brain structures.

Interestingly, leftward asymmetry was detected in caudate volumes of HCs. Physiological striatal asymmetry varies by sample, yielding an inconsistent pattern of results in the literature [35]. Physiological hemispheric asymmetry is often associated with several factors that could cause anatomical and functional lateralization of the brain, such as motor activity, aging and genetic factors [36]. In HD patients, no significant volume asymmetries were found in any of the basal ganglia structures, in agreement with the hypothesis that HD is a symmetric disease [17].

4.2 *NM-MRI Analysis*

The results obtained in the volumetry analysis revealed a significant reduction of volume in the midbrain of HD patients with respect to HCs. Furthermore, midbrain areas were significantly smaller in HD patients. Hence, it may not come as a surprise that SNc areas are also depleted in HD patients as a consequence of midbrain atrophy. However, the SNc ratio was significantly reduced in HD patients, suggesting that although midbrain atrophy plays a role in the reduction of SNc areas, it does not solely account for the observed depletion of NM-containing neurons in the SNc of HD patients.

While a reduction of SNc area in HD patients represents dopaminergic neuronal loss and thus NM depletion in this structure, other processes may be involved in pigment loss. Neurons that survive SNc atrophy in HD might still present reduced content of NM. The CR was thus used to quantify the distribution of this pigment in the SNc of HD and healthy subjects. No significant differences in the CR values of the SNc between the HD and HC groups. Nevertheless, SNc CR values of HD patients tended to be smaller than those of HCs. One possible factor affecting this analysis is the choice of reference ROI. In this study, the central regions of the *crus cerebri* were selected for the placement of two circular ROIs, as in [32] and in [37], while in other studies a single and larger reference ROI was placed in the decussation of the superior cerebellar peduncles [29],[38].

The correlations found between SNc ratio and the relative volumes of the caudate (0.58), putamen (0.66) and GP (0.67) of all subjects were all significant. These key outcomes suggest that a reduction in the SNc area, and thus a depletion of NM-containing neurons, is somehow related to basal ganglia atrophy in HD patients, which is an established feature of the disease. Dopaminergic projections from the SNc to the striatum play a modulatory role in the corticostriatal pathway, ultimately facilitating voluntary movement. Hence, a dysregulation of dopamine in this pathway could result in uncontrolled involuntary movements [9], which are major manifestations of HD. Indeed, in PD, selective degeneration of NM-containing nigrostriatal neurons, which is the hallmark of this disorder, leads to abnormalities in the dopamine metabolism, manifesting as bradykinesia, tremor and rigidity [39]. While the neuropathology and symptoms of HD differ from those of PD, both disorders arise from the accumulation of misfolded protein aggregates, suggesting at least some degree of similarity between underlying pathological processes, perhaps involving SNc degeneration and NM loss. However, it is not clear if this NM depletion in SNc would be a primary or secondary event in HD, nor if these changes would precede basal ganglia atrophy or result from such process. Longitudinal studies of NM-quantifying parameters are required to assess the time course of SNc degeneration in HD patients.

A significant and strong correlation was found between the SNc areas and the TFC (0.79) of HD patients, suggesting that depletion of NM-containing neurons might be one of the factors responsible for the decrease in functional capacity of these subjects.

The FSE NM-MRI imaging protocol used in this work had some limitations. Signal intensities of FSE acquisitions are not homogeneous due to the sensitivity to the RF field [40], which represents a subject-dependent confounding factor that cannot be accounted for with image filtering. Longer acquisition time and larger slice thickness were required to account for the relatively low SNR ratio of images obtained with this sequence. Furthermore, this imaging protocol had a long scan time (8 minutes), which may pose a critical problem when imaging patients with intense choreatic movements. In this study, 4 of the patients had early-stage HD (≤ 5 years of disease duration) and thus did not present strong involuntary movements, while the remaining 4 subjects had a disease duration of 10 or more years, corresponding to the disease stage when rigidity and movement impairment supervene. In the future, if 2D FSE sequences are to be used in NM-MRI analysis, the acquisition protocol should be optimized to reduce acquisition time and to improve image contrast, which might increase the sensitivity of CR measurements. Alternatively, 3D GE sequences with prepared MT contrast pulses, which generally have a much

lower acquisition time, may be used to evaluate high-signal SNc volumes and to calculate their CR three-dimensionally in NM-MR images as a more complete approach to NM quantification. While the measurement of SNc volumes with such GE sequences in NM-MR images has been applied in at least one study in PD [41], its feasibility still needs to be further confirmed and validated in HD.

Despite being accurate, less user-dependent and less time-consuming than manual segmentation, the SNc segmentation algorithm used in this work required manual seed point selection. While segmentation variability associated with seed point selection was not investigated, future studies should confirm the inter-rater reproducibility of this method. Fully automated NM-MRI segmentation and image analysis approaches are required to eliminate the inter-operator inaccuracies of manual and semi-automatic methods, while retaining measurement accuracy and reducing analysis time. For instance, an automated SNc segmentation with registration to a previously labelled atlas of the midbrain could prove to be feasible in NM-MR images, as it was done in [42] in a PD study.

4.3 *R_2*-Relaxometry Analysis*

No significant increases in iron content were detected in the basal ganglia of HD patients, although the R_2* values in the GP of HD patients tended to be larger than those of HCs. However, reports from other groups using several different MRI-based iron measures inconsistently indicate that one, two or all of these structures undergo significant iron deposition in HD patients. Electing a single method for MRI-based iron quantification in HD such as R_2* relaxometry, QSM or a combination of both, might aid in dissipating the variability of the results reported in the literature.

No significant correlations were found between R_2* values of the basal ganglia and their relative volumes, although there was a trend towards significance in the case of the correlation between caudate iron and volume. These findings suggest that basal ganglia atrophy and iron accumulation are independent processes, in agreement with an R_2* relaxometry study in HD [23]. On the other hand, significant inverse correlations were reported between iron and volume in the putamen and in the GP of HD patients in another R_2* study [24], while significant inverse correlations were found between the same parameters but in the caudate and putamen of premanifest HD patients in a QSM study [25]. On the other hand, the R_2* values of the GP and the TFC of HD patients correlated significantly (0.95), indicating that iron accumulation in this structure might underlie abnormalities in the functional capacities of these subjects.

4.4 *General Limitations and Future Work*

The main limitation of this study was the small number of HD patients (n=8) included in the clinical sample, which may have hindered several comparisons in this study, especially the correlations between the analyzed parameters and the clinical variables of these subjects, which did not always reach statistical significance. Reproducing these analyses in larger HD sample size is of upmost importance to confirm the results hereby obtained and, most of all, to verify the reliability of using NM-quantification parameters as biomarkers in this disease.

A confound factor transversal to all analyses was the effect of age on the measured parameters. Firstly, the caudate, putamen, GP and brainstem volumes decrease with age [43]. Moreover, there is a progressive accumulation of NM in the SNc [27] and an increase in the iron content of basal ganglia with age [44]. Since the mean age of HCs was significantly higher than that of HD patients, these effects might have introduced bias in all analyses. In future studies, age should be taken into account as a covariate to avoid such bias effects.

The CAG repeat number of HD patients and the scores of clinical scales other than the UHDRS MTS and TFC were not available in this study. CAG repeat size is the major determinant of age at onset, disease progression and age at death in HD, thus it would be interesting to relate the changes revealed in this study, especially the degeneration of the SNc, with this clinical parameter.

A histological study reported that the loss of pigmented neurons in the SNc of HD patients was more severe in the medial and lateral thirds of the SNc, while neurons in the central third of this structure were relatively spared [28]. In the future it might be interesting to study separately the CR in each of these subregions of the SNc in HD patients with NM-MRI in search for a possible pattern of NM depletion.

5. Conclusion

The use of high-resolution T_1-weighted imaging to quantify reductions in brain volumes has so far been considered the most suitable and sensitive MRI technique for the cross-sectional and longitudinal studies of HD. Indeed, volume reductions in the caudate, putamen, GP, brainstem and midbrain of HD patients were revealed in this work. However, in view of the clinical heterogeneity of the disease, a multimodal approach may offer a novel means of detecting simultaneous neurological changes that occur in the HD brain, in the search of biomarkers to find disease-modifying therapies. NM-MRI techniques previously applied for the quantification of NM in the SNc, mostly in PD patients, were for the first time employed in this work in HD. SNc areas of HD patients were significantly reduced and correlated with the volumes of the caudate, putamen and GP, suggesting at least a degree of dependence between NM depletion and basal ganglia atrophy. In turn, findings from HD studies may have key relevance for other more prevalent neurodegenerative disorders which share some pathological features with HD, such as AD and PD, for which highly predictive tests are not yet available.

6. References

[1] G. P. Bates *et al.*, “Huntington disease,” *Nat. Rev.*, vol. 1, pp. 1–21, 2015.

[2] S. S. Baig, M. Strong, and O. W. Quarrell, “The global prevalence of Huntington’s disease: a systematic review and discussion,” *Neurodegener. Dis. Manag.*, vol. 6, no. 4, pp. 331–43, 2016.

[3] The Huntington’s Disease Collaborative Research Group, “A novel gene containing a trinucleotide repeat that is expanded and unstable on Huntington’s disease chromosomes,” *Cell*, vol. 72, pp. 971–983, 1993.

[4] C. A. Ross, M. Kronenbuerger, W. Duan, and R. L. Margolis, “Mechanisms underlying neurodegeneration in Huntington disease: applications to novel disease-modifying therapies,” in *Handbook of Clinical Neurology*, 1st ed., vol. 144, A. S. Feigin, Ed. Elsevier B.V., 2017, pp. 15–28.

[5] C. A. Ross and S. J. Tabrizi, “Huntington’s disease: From molecular pathogenesis to clinical treatment,” *Lancet Neurol.*, vol. 10, pp. 83–98, 2011.

[6] B. Kremer *et al.*, “A worlwide study of the Huntington’s Disease mutation : the sensitivity and specificity of measuring CAG repeats,” *N. Engl. J. Med.*, vol. 330, no. 20, pp. 1401–1406, 1994.

[7] R. Reilmann, B. R. Leavitt, and C. A. Ross, “Diagnostic criteria for Huntington’s disease based on natural history,” *Mov. Disord.*, vol. 29, no. 11, pp. 1335–1341, 2014.

[8] J. P. Vonsattel, R. H. Myers, T. J. Stevens, R. J. Ferrante, E. D. Bird, and E. P. Richardson, “Neuropathological classification of Huntington’s disease,” *J Neuropathol Exp Neurol*, vol. 44, no. 6, pp. 559–577, 1985.

[9] K. D. Bunner and G. V Rebec, “Corticostriatal Dysfunction in Huntington’s Disease: The Basics,” *Front. Hum. Neurosci.*, vol. 10, no. 317, pp. 1–12, 2016.

[10] M. A. Nance and R. H. Myers, “Juvenile Onset Huntington’s Disease - Clinical and Research Perspectives,” *Ment. Retard. Dev. Disabil. Reseach Rev.*, vol. 7, pp. 153–157, 2001.

[11] A. M. Estrada-Sánchez and G. V. Rebec, “Role of cerebral cortex in the neuropathology of Huntington’s disease,” *Front. Neural Circuits*, vol. 7, no. 19, pp. 1–9, 2013.

[12] Huntington Study Group, “Unified Huntington’s disease rating scale: Reliability and consistency,” *Mov. Disord.*, vol. 11, no. 2, pp. 136–142, 1996.

[13] R. Reilmann and R. Schubert, “Motor outcome measures in Huntington disease clinical trials,” in *Handbook of Clinical Neurology*, 1st ed., vol. 144, Elsevier B.V., 2017, pp. 209–225.

[14] J. S. Paulsen *et al.*, “Challenges assessing clinical endpoints in early Huntington disease,” *Mov. Disord.*, vol. 25, no. 15, pp. 2595–2603, 2010.

[15] F. Niccolini and M. Politis, “Neuroimaging in Huntington’s disease,” *World J. Radiol.*, vol. 6, no. 6, pp. 301–312, 2014.

[16] R. I. Scahill, R. Andre, S. J. Tabrizi, and E. H. Aylward, “Structural imaging in premanifest and manifest Huntington disease,” in *Handbook of Clinical Neurology*, 1st ed., vol. 144, A. S. Feigin and K. E. Andreson, Eds. Elsevier B.V., 2017, pp. 247–261.

[17] H. D. Rosas *et al.*, “Striatal volume loss in HD as measured by MRI and the influence of CAG repeat,” *Neurology*, vol. 57, no. 6, pp. 1025–1028, 2001.

[18] M. Mascalchi *et al.*, “Huntington Disease: Volumetric, Diffusion-weighted, and Magnetization Transfer MR Imaging of Brain,” *Neurorad*, vol. 232, no. 3, pp. 867–873, 2004.

[19] H. D. Rosas, W. J. Koroshetz, Y. I. Chen, C. Skeuse, and M. Vangel, “Evidence for more widespread cerebral pathology in early HD,” *Neurology*, vol. 60, pp. 1615–1620, 2003.

[20] G. Douaud *et al.*, “Distribution of grey matter atrophy in Huntington’ s disease patients: A combined ROI-based and voxel-based morphometric study,” *Neuroimage*, vol. 32, pp. 1562–1575, 2006.

[21] C. Langkammer and N. Krebs, “Quantitative MR Imaging of Brain Iron : A Postmortem Validation Study,” *Radiology*, vol. 257, no. 2, pp. 455–462, 2010.

[22] C. Langkammer *et al.*, “Quantitative susceptibility mapping (QSM) as a means to measure brain iron? A post mortem validation study,” *Neuroimage*, vol. 62, pp. 1593–1599, 2012.

[23] C. Sánchez-Castañeda *et al.*, “Seeking huntington disease biomarkers by multimodal, cross-sectional basal ganglia imaging,” *Hum. Brain Mapp.*, vol. 34, pp. 1625–1635, 2013.

[24] C. Sánchez-Castañeda, F. Squitieri, M. Di Paola, M. Dayan, M. Petrollini, and U. Sabatini, “The role of iron in gray matter degeneration in huntington’s disease: A magnetic resonance imaging study,” *Hum. Brain Mapp.*, vol. 36, pp. 50–66, 2015.

[25] J. M. G. van Bergen *et al.*, “Quantitative susceptibility mapping suggests altered brain iron in premanifest Huntington’s disease,” *AJNR Am J Neuroradiol.*, vol. 37, no. 5, pp. 789–796, 2016.

[26] J. F. Domínguez D *et al.*, “Iron accumulation in the basal ganglia in Huntington’s disease: cross-sectional data from the IMAGE-HD study,” *J. Neurol. Neurosurg. Psychiatry*, vol. 87, no. 5, pp. 545–549, 2016.

[27] F. A. Zucca *et al.*, “Neuromelanin of the human substantia Nigra: An update,” *Neurotox. Res.*, vol. 25, pp. 13–23, 2014.

[28] K. Oyanagi, S. Takeda, H. Takahashi, E. Ohama, and F. Ikuta, “A quantitative investigation of the substantia nigra in Huntington’s disease,” *Ann. Neurol.*, vol. 26, pp. 13–19, 1989.

[29] M. Sasaki *et al.*, “Neuromelanin magnetic resonance imaging of locus ceruleus and substantia nigra in Parkinson’s disease,” *Neuroreport*, vol. 17, no. 11, pp. 1215–1218, 2006.

[30] B. Fischl *et al.*, “Whole Brain Segmentation: Neurotechnique Automated Labeling of Neuroanatomical Structures in the Human Brain,” *Neuron*, vol. 33, no. 3, pp. 341–355, 2002.

[31] J. E. Iglesias *et al.*, “Bayesian segmentation of brainstem structures in MRI,” *Neuroimage*, vol. 113, pp. 184–195, 2015.

[32] M. Carvalho, “Estudo Imagiológico em Ressonância Magnética de Doentes com Doença de Parkinson Late Stage,” Faculty of Sciences and Technology, NOVA University of Lisbon, 2016.

[33] J. M. Grilo, “NM-MRI for treatment evaluation of Parkinson’s Disease patients,” Faculty of Sciences and Technology, NOVA University of Lisbon, 2017.

[34] U. Rüb *et al.*, “Huntington’s disease (HD): Degeneration of select nuclei and widespread occurrence of neuronal nuclear and axonal inclusions in the brainstem,” *Brain Pathol.*, vol. 24, no. 3, pp. 247–260, 2014.

[35] F. M. Gunning-Dixon, D. Head, J. McQuain, J. D. Acker, and N. Raz, “Differential aging of the human striatum: A Prospective MR Imaging Study,” *Am. J. Neuroradiol.*, vol. 19, pp. 1501–1507, 1998.

[36] A. Elkattan, A. Mahdy, M. Eltomey, and R. Ismail, “A Study of Volumetric Variations of Basal Nuclei in the Normal Human Brain by Magnetic Resonance Imaging,” *Clin. Anat.*, vol. 30, pp. 175–182, 2017.

[37] S. Reimão *et al.*, “Substantia nigra neuromelanin magnetic resonance imaging in de novo Parkinson’s disease patients,” *Eur. J. Neurol.*, vol. 22, no. 3, pp. 540–546, 2015.

[38] C. Ohtsuka *et al.*, “Differentiation of early-stage parkinsonisms using neuromelanin-sensitive magnetic resonance imaging,” *Park. Relat. Disord.*, vol. 20, no. 7, pp. 755–760, 2014.

[39] D. W. Dickson, “Neuropathology of Parkinson disease,” *Park. Relat. Disord.*, vol. 46, pp. S30–S33, 2018.

[40] K. Ogisu *et al.*, “3D neuromelanin-sensitive magnetic resonance imaging with semi-automated volume measurement of the substantia nigra pars compacta for diagnosis of Parkinson’s disease,” *Neuroradiology*, vol. 55, no. 6, pp. 719–724, 2013.

[41] X. Chen *et al.*, “Simultaneous imaging of locus coeruleus and substantia nigra with a quantitative neuromelanin MRI approach,” *Magn. Reson. Imaging*, vol. 32, pp. 1301–1306, 2014.

[42] G. Castellanos *et al.*, “Automated Neuromelanin Imaging as a Diagnostic Biomarker for Parkinson’s Disease,” *Mov. Disord.*, vol. 30, no. 7, pp. 945–952, 2015.

[43] K. B. Walhovd *et al.*, “Effects of age on volumes of cortex, white matter and subcortical structures,” *Neurobiol. Aging*, vol. 26, no. 9, pp. 1261–1270, 2005.

[44] D. Aquino *et al.*, “Age-related Iron Deposition in the Basal Ganglia: Quantitative Analysis in Healthy Subjects,” *Radiology*, vol. 252, no. 1, pp. 165–172, 2009.